LAWRENCE
LIVERMORE
NATIONAL
LABORATORY

LLNL-JRNL-605092

Detailed Implosion Modeling of DT-Layered Experiments on the National Ignition Facility

D. S. Clark, D. E. Hinkel, D. C. Eder, O. S. Jones, S. W. Haan, B. A. Hammel, M. M. Marinak, J. L. Milovich, L. J. Suter, R. P. J. Town

November 29, 2012

Physics of Plasmas

Disclaimer

This document was prepared as an account of work sponsored by an agency of the United States government. Neither the United States government nor Lawrence Livermore National Security, LLC, nor any of their employees makes any warranty, expressed or implied, or assumes any legal liability or responsibility for the accuracy, completeness, or usefulness of any information, apparatus, product, or process disclosed, or represents that its use would not infringe privately owned rights. Reference herein to any specific commercial product, process, or service by trade name, trademark, manufacturer, or otherwise does not necessarily constitute or imply its endorsement, recommendation, or favoring by the United States government or Lawrence Livermore National Security, LLC. The views and opinions of authors expressed herein do not necessarily state or reflect those of the United States government or Lawrence Livermore National Security, LLC, and shall not be used for advertising or product endorsement purposes.

Detailed implosion modeling of deuterium-tritium layered experiments on the National Ignition Facility

D. S. Clark, D. E. Hinkel, D. C. Eder, O. S. Jones, S. W. Haan,
B. A. Hammel, M. M. Marinak, J. L. Milovich, H. F. Robey, L. J. Suter, and R. P. J. Town

Lawrence Livermore National Laboratory
Livermore, CA 94550

This work was performed under the auspices of the U.S. Department of Energy by Lawrence Livermore National Laboratory under Contract DE-AC52-07NA27344.

Abstract

More than two dozen Inertial Confinement Fusion (ICF) ignition experiments with cryogenic DT layers have now been performed on the National Ignition Facility (NIF) [G. H. Miller, E. I. Moses, and C. R. Wuest, Opt. Eng. **443**, 2841 (2004)]. Each of these yields a wealth of data: neutron yield, neutron down-scatter fraction, burn-averaged ion temperature, x-ray image shape and size, primary and down-scattered neutron image shape and size, etc. Compared to 2-D radiation-hydrodynamics simulations modeling both the hohlraum and the capsule implosion, however, the measured capsule yield is usually lower by a factor of five to ten, and the ion temperature varies from simulations, while most other observables are well matched between experiment and simulation. In an effort to understand this discrepancy, we perform detailed post-shot simulations of a subset of NIF implosion experiments. Using two-dimensional HYDRA simulations [M. M. Marinak, *et al.*, Phys. Plasmas **8**, 2275 (2001).] of the capsule only, these simulations represent as accurately as possible the conditions of a given experiment, including the as-shot capsule metrology, capsule surface roughness, and ice layer defects as seeds for the growth of hydrodynamic instabilities. The radiation drive used in these capsule-only simulations can be tuned to reproduce quite well the measured implosion timing, kinematics and low-mode asymmetry. In order to simulate the experiments as accurately as possible, a limited number of fully three-dimensional implosion simulations are also being performed. Despite detailed efforts to incorporate all of the effects known and believed to be important in determining implosion performance, substantial yield discrepancies remain between experiment and simulation. Some possible alternate scenarios and effects that could resolve this discrepancy are also discussed.

I. INTRODUCTION

Inertial Confinement Ignition (ICF) ignition experiments [1, 2] have been underway on the National Ignition Facility (NIF) [3] since June of 2011. In each of these experiments, a layer of cryogenic DT (deuterium-tritium) fuel is compress via x-ray ablation of a surrounding plastic ablator driven by 1.2 – 1.6 MJ of laser energy directed into a gold or uranium hohlraum [4]. The goal of these experiments is to trigger propagating thermonuclear burn of the DT fuel from a central, low-density hot spot with temperatures in the range of a few keV into a denser shell of surrounding cold fuel at densities of ~ 1,000 g/cm^3 [5, 6]. To date, twenty-nine pulse-shaped implosion experiments have been conducted on NIF using cryogenic fuel layers with a range of laser powers, laser pulse durations, hohlraum materials and geometries, and also capsule dimensions and capsule dopant compositions.

In parallel to the experimental work of fielding, firing, and diagnosing ignition experiments on NIF, an extensive analysis effort has been underway to interpret the data flowing from these experiments, compare it to the results of simulations used in designing experiments for NIF, and understand the implications for future experiments and the ongoing ignition campaign. By any measure, ignition experiments on NIF are highly integrated in nature, incorporating as they do the complex physics of laser propagation and conversion to x-rays, x-ray driven ablation of the capsule outer surface, the growth of hydrodynamic instabilities during the capsule implosion to high density, and finally nuclear reactions and, hopefully, burn propagation from the high temperature hot spot. Given this highly integrated nature, heavy reliance must be made on sophisticated numerical simulations for interpretation of and comparison to experimental data. In this respect, dedicated efforts have been underway through the duration of the ignition campaign to run detailed post-shot simulations of a significant number of the ignition experiments fielded on NIF.

In broad terms, simulations of NIF ignition experiments may be classified into two categories: integrated hohlraum simulations and capsule-only simulations. As the name implies, integrated hohlraum simulations aim to model all of the relevant physics processes in a NIF implosion experiment, from laser propagation into the hohlraum to conversion to x-rays, and finally to stagnation and burn of the imploded capsule. Given that computation resources are inevitably finite, however, a simulation that includes all of these physics processes will necessarily do so at reduced resolution for each individual process. In particular, the majority of hohlraum simulations are run with inadequate resolution to model the effects of short wavelength hydrodynamic instability growth in the imploding capsule [7], namely the Rayleigh-Taylor [8, 9] and Richtmyer-Meshkov [10, 11] instabilities. These simulations are predominantly also run in an axisymmetric, two-dimensional (2-D) approximation. The alternative to integrated hohlraum simulations that attempts to capture the effects of hydrodynamic instability growth is capsule-only simulation. In this approach, only the imploding capsule is modeled with the surrounding hohlraum replaced by a source region for an imposed x-ray drive. Simulations of this type are routinely run with resolution sufficient to model the growth of surface perturbations at scales corresponding to Legendre eigenmodes as high as 1,000 in 2-D and in a few cases in 3-D at comparable resolution [13, 15].

In a post-shot mode, hohlraum simulations have frequently used laser power inputs that are adjusted compared to the known laser input in order to reproduce some measured feature of the experiment being simulated, *e.g.*, time of peak neutron production or implosion velocity [16]. In an analogous manner, capsule-only simulations can use adjusted x-ray drives that are "tuned" to reproduce observed implosion performance. For the purpose of post-shot capsule simulations, then, the x-ray drive on the capsule is treated as an adjustable parameter to be modified as necessary to reproduce the implosion characteristics already measured in experiment. The goal here is to

reproduce as closely as possible the known implosion dynamics, and then investigate the simulation's prediction of the unobserved features of the implosion, in particular the details of hydrodynamic instability growth. Post-shot simulations naturally also use whatever information is available on capsule and hohlraum metrology prior to the shot, and in the case of detailed capsule-only simulations, are run using measured surface finishes as seeds to hydrodynamic instability growth.

The objective of the detailed post-shot simulation effort has been to make a best attempt to include all effects known and believed to be important to a specific NIF ignition experiment to establish a baseline for comparison with the data. Only once all of these known effects have been included in a single simulation model, does it become meaningful to pose the question: How well or poorly do the results from ignition experiments compare to simulation? In particular, how well do they compare to simulations run following the same methodology used in developing the ignition point design and what guidance does this offer for future experiments? To the extent that discrepancies exist between experiment and detailed simulations, the post-shot simulations also inform what alternate scenarios may need to be invoked to resolve those deficits. It has been found over the ensemble of post-shot simulations discussed below that many—though not all—of the observations from NIF ignition experiments can be reproduced in detailed simulations. In particular, it is found that simulations consistently over predict observed neutron yields by factors of five to ten.

This paper is organized as follows. Sec. II describes the ingredients and limitations of the standardized post-shot capsule model. This includes the essentially 1-D "tuning" of the implosion via adjustments to the x-ray drive to reproduce observed implosion dynamics, the inclusion of 2-D asymmetry effects as the seeds for hydrodynamic instability growth, and some numerical details of the baseline post-shot simulation model. Sec. III then summarizes the results of post-shot simulations as compared to observation across a range of implosion experiments. Given the continuing discrepancies

between simulation and experiment, Sec. IV discusses possible alternate effects that, if included, could resolve the remaining discrepancies. As a specific example, Sec. V describes preliminary results from 3-D post-shot capsule simulations, and Sec. VI concludes.

II. STANDARDIZED POST-SHOT CAPSULE SIMULATION MODEL

Detailed post-shot capsule simulations have been run of a subset of NIF ignition experiments beginning in June 2011. Only simulations of shots since January 2012 will be discussed here, however, and the characteristics of these shots are summarized in Table 1. These seven shots ranged over various pulse shapes and hohlraum materials, various peak laser powers, and various capsule dopant concentrations. For each shot, an individual post-shot x-ray drive was generated and the appropriate capsule metrology data was used. As an example of the procedure followed to produce a detailed post-shot model for each shot, the shot fired on Feb. 5, 2012 (N120205) will be discussed in detail in this section. The following section will then discuss the results from the whole ensemble of shots simulated.

A. Effective capsule radiation drives

The first ingredient in the post-shot simulation model is a radiation drive tuned to match the observed 1-D implosion characteristics. The capsule implosion characteristics on NIF have been measured using two complementary platforms: a Velocity Interferometer System for an Arbitrary Reflector (VISAR) platform [17, 18] used to measure shock break out times and velocities during the initial phase of a NIF implosion, and a Convergent Ablator (ConA) platform utilizing backlit radiography to measure the implosion trajectory and velocity during the later phase of the implosion [19, 20]. From the perspective of post-shot simulations, as illustrated in Fig. 1, the data from the VISAR platform constrains the forward part of the adjusted radiation drive up until the approximately

20 ns, while the data from the ConA platform, coupled with the observed time of peak neutron production (bang time), constrains the peak of the x-ray drive from 20 ns until the end of the drive. As shown in Fig. 1(b), by suitable adjustment to the incident x-ray drive or radiation temperature (Fig. 1(a)), the shock velocity measured by VISAR can be matched to essentially arbitrary accuracy in 1-D simulations with the radiation hydrodynamics code HYDRA [21]. This procedure of matching the VISAR data by making adjustments to the drive was pioneered in Ref. [18]. In the figure, the measured VISAR shock velocity for shot N120108 is shown by the black trace, and the simulated VISAR trace from a 1-D adjusted simulation is given by the red trace. The abrupt steps in the shock speed indicate the break out of the first shock from the CH ablator into the surrogate deuterium fuel followed by the overtaking of the leading shock by a following, stronger shock. The inset in the figure gives an example of the raw VISAR data used to extract shock timing and velocity. The error bars on the VISAR measurement are of the order of 50 ps in timing and 0.3 cm/μsec in velocity; the simulated trace follows the data within these error bars for all times. Likewise, Fig. 1(c) shows that similarly close agreement can be arranged between the observed shell implosion trajectory from a ConA measurement (black dots) and the simulated center of mass implosion trajectory from an adjusted 1-D simulation (red line). Note that this ConA simulation uses the same early-time pulse shape as already constrained by matching the VISAR trace. The inset again gives an example of the raw backlighting data used to extract the shell-averaged implosion trajectory.

Note that this procedure of combining data from a VISAR measurement and a ConA measurement to infer the implosion trajectory from a corresponding DT ignition experiment effectively combines the implosion characteristics of three separate shots (here N120108, N120122, and N120205). In principle, these three shots were fired with different laser powers and could also have suffered different levels of laser backscatter from the hohlraum. While effort is made to pair the most

appropriate VISAR and ConA shots to each DT shot, inevitable variability in laser performance between shots and variations in laser backscatter are always present. This variation in delivered laser power (due to intent and due to unintended backscatter) can be expected to produce shifts in the radiation temperature in the hohlraum by a non-negligible amount. To capture this effect in producing a final adjusted drive for each DT shot, ratios of x-ray fluxes from standardized post-shot hohlraum simulations using the as-shot laser powers and as-measured backscatter energies are used to translate the adjusted drives from the VISAR shot to the ConA shot and finally to the DT shot.

It is important to emphasize here that these adjusted x-ray drives should not be interpreted as an accurate representation of the radiation field inside of the hohlraum for any given implosion experiment. In the context of post-shot modeling, they are interpreted merely as effective radiation drives. That is, the drive represents whatever hohlraum or ablator physics is not currently being captured in nominal hohlraum or capsule simulations, for example, inaccuracies in hohlraum x-ray conversion efficiency or capsule ablator opacity. The purpose of these adjusted capsule drives is, again, merely to reproduce as closely as possible the observed dynamics of a particular NIF implosion so as to provide the most accurate vehicle for simulating the subsequent implosion performance, in particular hydrodynamic instability growth, fuel compression, and thermonuclear yield. While modifications could be made directly to the underlying physics processes used in these simulations, for example modifying the opacities or equations of state used in the simulation without modifying the x-ray drive, to improve agreement with the data, adjusting the drive provides the simplest and most direct means for altering the simulations so as to agree with the data. It should also be noted that, while the effective drive is heavily constrained, particularly by the early-time VISAR data, it is not unique, and various drives can be found that yield various levels of agreement with experiment,

especially with the late time ConA data. Influenced by the constraint of selecting a physically plausible drive profile, a measure of choice was exercised in determining the appropriate drive to use.

In addition to measuring the shell implosion trajectory as shown in Fig. 1(c), several other implosion characteristics are also inferred from the ConA backlit data, including the shell remaining mass fraction, the shell peak density, and the shell inflight thickness. The shell implosion velocity can also be inferred from the time derivative of the implosion trajectory. As shown in Fig. 2(a – d), the adjusted x-ray drive can also bring 1-D simulations into reasonable agreement with each of these observations. In each case, the black dots with error bars are the data, and the red curve is the corresponding simulated quantity. Note that the experimental data being matched is, of course, measured in three-dimensional reality, and the observed implosion characteristics could therefore be influenced by some amount of 2-D/3-D instability development. Late time thickening of the shell, as seen in Fig. 2(d), in particular could be associated with 3-D distortion or breakup of the shell. That a close match can be made with the data using only 1-D simulations, however, suggests that effects other than 2-D/3-D instabilities could account for the observed implosion dynamics, and 2-D simulations using the as-shot ConA surface finishes suggest that there should not be substantial shell thickening due to instabilities. On the other hand, as discussed below, the yield data from DT implosions appears to be more consistent with simulations with large amounts of instability growth. In this case, the ConA data should arguably be matched only in 2-D simulations allowing for large amounts of instability growth and could possibly result in the selection of a different adjusted radiation drive. Given the computational cost of this procedure, however, this approach has not been followed, and only 1-D tuned drives have been used. This ambiguity underscores the inevitable degree of non-uniqueness inherent in the adjusted drives.

Finally, in addition to matching the measured implosion characteristics from VISAR and ConA experiments, the 1-D drive is also adjusted, as necessary, to match the time of peak neutron production (bang time) and the neutron down-scattered ratio (DSR) in the DT implosion. The latter is defined as the ratio of the number of neutrons in the 10 – 12 MeV band of the neutron energy spectrum (the down-scattered energy range) to the number in the 13 – 15 MeV band (primary neutrons from DT fusion reactions) and is proportional to the overall compression or ρR of the final DT fuel assembly [22]. For all of the shots listed in Table 1, it was possible to match the DT bang time within its 60 ps error bar as well as the DSR within its shot dependent error while maintaining comparable agreement with the associated VISAR and ConA data, as shown in Figs. 1 and 2.

B. Capsule surface finishes

Once an effective radiation drive has been generated for each post-shot simulation, the next ingredients in the post-shot simulation model are the various surface finishes on each interface of the capsule that serve as seeds to hydrodynamic instability growth. Again, using N120205 as an example, Fig. 3 shows the inner ice surface roughness as a function of Legendre mode number (a) and the measured ablator outer surface roughness also as a function of mode number (b). The ice roughness is measured from three different directions immediately prior to the shot by x-ray imaging of the DT ice-gas interface [23], and the average of the three spectra is used to initialize the ice roughness in the post-shot simulations. The outer ablator surface roughness is measured by atomic force microscopy (AFM) of the ablator shells prior to assembly over eighteen meridians and one equatorial trace [24]. Like the ice surface, the average power spectrum of these nineteen traces is used to initialize the outer surface roughness in simulations. Note that, in both cases, except for a narrow band at $\ell \sim 20$ in the ablator surface roughness, both surfaces are considerably smoother than required by the ignition point design specifications [4]. Though it cannot be measured directly, surface roughnesses are also

initialized on all of the internal capsule layers in simulations: the interface between the DT fuel and ablator and all of the interfaces between the various dopant layers in the shell. According to previous practice [15], fractions of the measured outer surface roughness are initialized as roughness on each successive internal surface representing the incremental nature with which the capsule layers are deposited during fabrication.

In addition to broad-spectrum roughness, various localized defects are also present on capsule surfaces. On the DT inner surface there can be a number of localized cracks or grooves generated at crystal boundaries. While these inherently 3-D structures cannot effectively be modeled in the 2-D baseline simulations (see Sec. V), standardized simulations have included a 2-D representation of the largest ice groove observed on the fuel layer at a representative polar angle of 60°. Localized defects in the form of bumps or divots also exist on the ablator surface. These defects are typically too narrow in spatial extent to be modeled in baseline simulations but must be treated in more specialized, higher resolution simulations. A higher resolution feature that can also not be captured in the baseline simulations is the perturbation generated by the glass fill tube attached to the capsule. A surrogate for this effect, however, is included in the form of 30 ng of pre-loaded ablator material mixed into the central DT gas cavity as representing the effective mix observed in higher resolution simulations [12, 13].

Finally, the growth of perturbations at Legendre mode numbers less than ~ 6 is dominated by the 2-D and 3-D radiation drive asymmetries present in the hohlraum. To include this effect, the $\ell = 2 - 6$ flux asymmetries from post-shot hohlraum simulations are applied to the capsule radiation drive. Finally, the perturbation caused to the implosion by the formvar support tent used to hold the capsule in the center of the hohlraum is modeled by adding the thickness of the tent to the total ablator thickness in the region of the capsule where the tent attaches to the capsule at each pole. Higher

resolution simulations have suggested that this is an adequate model, though, according to simulations, the presence of the tent is a only very minor effect on the final implosion shape.

C. Post-shot capsule simulation numerical details

Using the above ingredients as inputs to the simulations, the baseline simulations for comparison with NIF implosion performance have been 2-D HYDRA simulations covering 180° in polar angle with sufficient resolution to model perturbations at scales down to Legendre mode numbers of $\ell = 100$. This resolution entails zoning of typically 450 x 1,000 zones in radius and angle. The simulations use multi-group diffusive radiation transport with sixty radiation groups, single-group electron and ion conduction, tabular equations of state and opacities, and particle Monte Carlo for transporting thermonuclear burn products.

For each implosion simulated, the simulations have been run in triplicate using three different random realizations of the surface roughness in order to gauge any variability in performance between realizations. The results for these three different realizations for N120205 are shown in Fig. 4 at bang time. In each case, the upper half of the plot shows material density and the lower half shows material region with dark blue denoting the DT fuel and the other colors the various layers of doped ablator. The red curve in each approximately demarcates the hot spot boundary according to a standardized definition [14]. Some slight variability is evident in the short wavelength hot spot shape between realizations, but the (deterministic) low-mode shape appears to dominate.

Several simulated experimental observables for these three different realizations are summarized in Table 2. The first four rows list the lowest order Legendre moments from simulated equatorial x-ray emission. The fifth row gives the simulated neutron down-scatter ratio (DSR), and the sixth row the ion temperature as inferred from Doppler broadening of the emitted neutron spectrum. The final row gives the neutron yield in the 13 – 15 MeV energy range. While there is some variability in the x-

ray shape moments above $\ell = 2$, the hot spot size, as reflected by P_0, the DSR, ion temperature, and yield all vary little between different realizations. In the far right column, the corresponding results from experiment are tabulated for each observable. The agreement is reasonable for the hot spot shape and DSR but somewhat discrepant in the ion temperature and discrepant by a factor of three in the neutron yield. This mix of agreement and disagreement between data and simulation will proved to be consistent across the whole ensemble of shots simulated as discussed in the following section.

III. COMPARISON OF POST-SHOT SIMULATIONS RESULTS WITH DATA

Returning from the specific case of shot N120205 to the entire ensemble of shots simulated from 2012, Fig. 5 plots the four principal observables (DSR, ion temperature, hot spot size, and neutron yield) as a function of shot number. In each panel, the data are shown as the black symbols with error bars and the simulation results are given by the red symbols. The error bars in the case of the simulation results give the RMS variation between the three different roughness realizations discussed in Sec. II. In most cases, these error bars are smaller than the size of the symbols. Immediately evident in the figure is that the simulations match reasonably well both the DSR values and the hot spot size or P_0. Some shots are out side of the error bars, but the data trends are reasonably well captured. Note, however, that the agreement with the DSR values is by design: the 1-D x-ray drive was adjusted so as match the observed DSR, and any discrepancy in Fig. 5 reflects the variability introduced by including 2-D roughness.

The agreement between data and simulation is less favorable for the ion temperature and neutron yield. For several experiments, the simulated ion temperatures are reasonably close, but for three shots in particular (N120213, N120311, and N120405) the observed ion temperatures are well below simulations. The yields are discrepant by a factor of several for all of the shots, but notably more so

for the three shots that show particularly low ion temperatures. On account of the low ion temperatures and particularly low yields, as well as particularly high x-ray radiated energies, for these shots, these experiments have been interpreted as exceptionally "high mix" shots in which large amounts of ablator material have contaminated the hot spot causing the hot spot to radiatively cool and the yield to drop.

The results shown in Figs. 4 and 5 were all computed with α-particle energy and momentum deposition switched off in the simulations. For purposes of comparing simulated observables (particularly simulated x-ray images and burn-averaged ion temperatures) with experiments in the low yield range of current experiments, this is a reasonable expediency as the effect of α -particle deposition and bootstrap heating in the simulation would otherwise produce very different diagnostic signatures compared to experiment. For completeness, however, simulations were run with α-particle deposition included as well as switched off as shown in Fig. 6. The inclusion of α-particle deposition (blue symbols) raises the simulated yields by roughly a factor of two indicating that the fuel configuration in the simulations is at the threshold for α-particle bootstrap heating. The experimental yields are evidently still a factor of a few below that threshold. Shown in Fig. 6(b) is the ratio of experimental yield to 2-D simulated yield with α-particle deposition both included and switched off. The dashed horizontal lines give the averaged ratio of experiment to simulation across all of the shots simulated with α-particle deposition included (blue) and with α-particle deposition switched off. With α-particle deposition included the average is 8%, and with α-particle deposition switched off the average is 16%.

IV. EFFECTS NOT INCLUDED IN CURRENT POST-SHOT SIMULATIONS

The simulation methodology described in Sec. II and compared to several NIF experiments in Sec. III represents the best practicable effort to simulate the performance of these shots including all the effects known and believed to be important. Despite this effort, discrepancies clearly remain with the data, particularly in terms of the neutron yield. Of course, as in any simulation model, approximations and compromises have been made in the simulations described above, and it is worth enumerating what effects have been neglected that could resolve the remaining differences.

The first and most obvious limitation of the simulations is resolution. The simulations described above included adequate zoning to resolve Legendre modes up to $\ell = 100$. For the perturbation spectra shown in Fig. 3, doubling the resolution up to $\ell = 200$ was found not to alter the results in any significant way. Given the added computational cost of resolving $\ell = 200$, this convergence study motivated running all of the simulations discussed in Sec. III using $\ell = 100$ resolution. On the other hand, not included in the spectral roughness shown in Fig. 3 are known localized defects or bumps on the ablator surface requiring resolutions of $\ell \sim 500$ to simulate accurately [26]. Closely related to these ablator surface defects, small amounts of "dust" or debris are also known to be present on the ablator surface on some shots. This dust is predominately believed to be flakes of organic material (similar in composition to the ablator itself) or fragments of aluminum as a residual from the capsule handling process. The latter type of dust can, in simulations, produce very large jets that, like the fill tube or ablator defects, inject large amounts of doped ablator material into the hot spot. Given the very high computational cost of simulating the effects of defects or dust, etc., such effects can only be treated on an individualized basis and are the subject of ongoing work. The added ablator mix into the hot spot that could be caused by such surface defects and debris, however, is almost certainly a contributor to the lower than simulated yields discussed above.

While more highly resolved simulations than those described here are required to model the impact of defects and debris in detail, simple surrogates for these effects can be added to current simulations in an effort to understand scalings and sensitivities. As a surrogate for enhanced mixing, the roughness seeds used in the above simulations can simply be increased to assess the impact of substantially enhanced mix on simulated observables (potentially due to ablator defects or debris). Fig. 7 shows the scaling of the four principal observables as the ablator surface roughness is increased up to five times the measured value. In this case, the shot N120321 was used as the baseline. In each panel (a) – (d) of the figure, the pink band gives the measured value of the particular observable, while the insets show the imploded core configuration with both nominal ablator roughness and five times the nominal roughness. These simulations, and those shown in Fig. 8 below, include a-particle deposition. With five times the nominal roughness, the simulations match the neutron yield, ion temperature, and approximately match the hot spot size. As the inset makes evident, however, the enhanced mixing has caused the shell entirely to break apart leading to a substantial reduction of the DSR below the measured value. Recall, however, that the 1-D (unperturbed) simulation was adjusted to match this measured value. Had the 1-D simulation been adjusted to overshoot the measured DSR, it is conceivable that the 2-D simulation with enhanced roughness could match all four observables simultaneously. This level of agreement remains to be demonstrated, but these simulations do suggest that the observed performance of experiments could be consistent with enhanced mix.

As a surrogate for the ablator material that can be injected deep into the hot spot due to localized jets caused by ablator surface defects or debris, simulations may also be run with enhanced pre-loaded mix of ablator material into the central DT gas. As described in Sec. III, this pre-loading of ablator material into the DT gas is already used as a surrogate for the effect of the fill tube. Fig. 8 plots simulated outputs for N120321 as a function of pre-loaded ablator mass in the DT gas. As Fig. 8(a)

shows, ~ 1,000 ng of pre-loaded ablator mass brings the simulation into agreement with the observed yield. The disagreement with the other observables clearly makes this scenario less plausible in explaining observations. As pointed out in Sec. III, however, a subset of shots (although not N120321) show low ion temperatures and low yields not inconsistent with the scaling shown here. Evidently, the injection of substantial amounts of ablator material into the hot spot could be consistent with observations from these shots. Note, of course, that the two alternate scenarios explored here, enhanced ablation front instability growth and enhanced injection of ablator material into the hot spot, need not operate in isolation and that some combination of these two effects, as well as others, are likely present to varying degrees on all shots.

In addition to resolution, the dimensionality of the simulations is also approximate. All of the simulation results presented above assumed a 2-D, axisymmetric approximation. As already emphasized in the case of grooves or cracks in the DT fuel layer, however, a number implosion perturbation seeds are inherently 3-D in nature. In addition to grooves, this list includes clusters of bumps on the ablator surface or scratches on the ablator, as well as 3-D asymmetries in the radiation field in the hohlraum due to imperfections in the delivered laser illumination pattern or diagnostic ports in the hohlraum walls. Furthermore, sufficiently rapid growth of even uncorrelated perturbations can cause those perturbations to reach nonlinear amplitudes at which point the growth in 3-D reality will be more rapid than in a 2-D approximation. The importance of all of these effects in potentially resolving remaining discrepancies motivates running 3-D post-shot simulations. Progress on these 3-D simulations is discussed in detail in the following section.

Beyond numerical considerations of resolution and dimensionality, an additional and likely important effect has recently come to light that is not included in the current simulations. As described in the companion papers, neutron imaging from NIF implosions [27], neutron spectroscopy

from NIF implosions [28], and also a thermodynamic model fit to various x-ray and nuclear observables from NIF implosions [29] all suggest the presence of large low-mode asymmetries in the cold compressed fuel that are not manifest in the x-ray images from the hot spot. Recent simulation scoping studies [30, 31] suggest that such "unseen" low-mode asymmetries ($\ell = 1 - 4$) in the fuel can lead to substantial degradation in the yields while maintaining plausible agreement with measured ion temperatures and low-mode x-ray shape measurements. These results are preliminary, and the neutron imaging and spectroscopy measurements that underlie them continue to be analyzed, but such low-mode effects could resolve the remaining discrepancies seen in Fig. 5. A particular question to be answered is whether, given the limited sampling in solid angle that these nuclear measurements use, the perceived mode $\ell = 1$ or 2 perturbation extracted from the data does not in reality represent aliasing from a higher mode such as could result from vigorous shorter wavelength instability growth.

V. 3-D FULL SPHERE SIMULATION

To address the importance of 3-D effects in resolving the continuing discrepancy between experiment and simulation, an exploratory 3-D simulation was run of the N120205 shot. In addition to the presence of 3-D defects as seeds of instability growth, 3-D simulations—particularly simulations of the full sphere—were motivated by the removal of the artificial symmetry constraints that apply in 2-D axisymmetric simulations or even 3-D subsector simulations. In 2-D axisymmetric simulations or 3-D subsector simulations, the flow in the central hot spot is constrained from crossing the symmetry axis or a central point in 3-D producing an artificial stagnation effect. In 3-D reality, of course, this constraint does not apply, and material may flow through the hot spot center in an essentially arbitrary fashion. The only means of capturing this effect is a by simulation that models

the full sphere. The added effects of 3-D vortex stretching and kinking can also only be modeled in 3-D simulations, effects that are crucial in modeling the transition to 3-D turbulence.

Since a 3-D model of the implosion necessitates no approximation of the surface perturbations as is done in 2-D, the capsule surface metrology up to $\ell = 50$ was applied directly to the ablator surface in the 3-D simulation. This includes both low-mode AFM data ($\ell < 20$) [24], and higher-mode PSDI data ($\ell > 20$) [25]. Likewise, the observed grooves seen in images of the DT fuel layer taken prior to the shot were initialized at the DT ice-gas boundary in the simulation. Broad-spectrum 3-D roughness corresponding to the three-view averaged power spectrum from Fig. 3(a) was also included, as well as power-spectrum roughness on the internal capsule interfaces. Finally, a 3-D analogue of the support tent perturbation used in 2-D was applied, and 3-D x-ray drive asymmetries were also included as extracted from a companion 3-D hohlraum simulation. Fig. 9 shows 3-D renderings of the initial perturbations to the DT ice-gas boundary (a), including several ice grooves, and the initial outer ablator surface (b), including localized surface bumps, lower mode modulations, and the support tent. Due to the computational cost, this initial 3-D simulation was run at only half the resolution of the corresponding 2-D simulations. Even so, this simulation required 100 million computational zones and 2 million CPU hours to complete. A 3-D simulation with resolution of $\ell = 100$ equal to the 2-D simulations is in progress.

Fig. 10 shows a rendering from this simulation at bang time. The cutaway green surface shows the interface between the DT fuel and the plastic ablator, and the enclosed red surface shows the 1.0 keV ion temperature isosurface, an approximate surrogate for the boundary between the low density hot spot and the high density cold shell. The large spike-like structures in the fuel-ablator interface correspond to the largest ablator surface defects that have grown to a highly nonlinear stage. Despite their large amplitudes, these spike-like structures do not succeed in injecting ablator material into the

hot spot for the mode range simulated. The red hot spot boundary is strongly distorted and highly 3-D in character but clearly dominated by longer wavelength distortions than the fuel-ablator interface. This results from the usual effects of short wavelength attenuation for modes feeding in from the outer layers as well as ablative stabilization of perturbations growing directly at the hot spot boundary. In this simulation, the positive z-axis is aligned with the upward-pointing hohlraum axis.

In Fig. 11(a), a slice through the 3-D simulation aligned with the hohlraum axis is shown where the color scale gives the mass density at the same time as shown in Fig. 10. Panel (b) shows the corresponding 2-D simulation result on the same color scale at its neutron bang time. The 3-D simulation shows the anticipated longer growth of Rayleigh-Taylor spikes penetrating into the hot spot and bubbles rising into the dense shell. Along the negative z-axis, a large bubble can be seen nearly breaking through the surrounding shell. The rather low mode character of the hot spot shape ($\ell = 10 - 20$) is evident in both 3-D and 2-D. Fig. 12 illustrates another interesting feature of the 3-D simulation by comparing the material flow speeds between 3-D and 2-D. On account of the absence of the artificial symmetry constraints, the 3-D simulation develops a more complex, turbulent-like flow pattern with flow velocities of ~ 400 μm/ns, nearly twice those of the 2-D simulation. This higher hot spot flow velocity can have two important effects on the observables of the implosion: First, the higher flow speeds represent inflowing implosion kinetic energy that was not successfully converted to compression energy or hot spot heating. As such, it represents a loss mechanism for implosion efficiency. Second, via the Doppler effect, this higher flow velocity can also contribute to a higher observed ion temperature as inferred from the broadening of the primary neutron spectrum.

Table 3 summarizes the simulation results for N120205 as a function of dimensionality with both α-particle deposition included and switched off and as compared to the data. Encouraging trends with respect to matching the data are evident in several of the observables as the simulation fidelity is

increased from 1-D simulations through 3-D simulations. In particular, ion temperatures and inferred hot spot residual (*i.e.*, un-stagnated) kinetic energies increase towards the data in going from 1-D to 3-D, while inferred hot spot pressures and yields drop. While the ion temperature and inferred residual kinetic energy are quite close to the data for the 3-D simulation without α-particle deposition, the inferred hot spot pressure and yield still remain significantly higher than the data.

VI. CONCLUSIONS

This paper has summarized the status of detailed post-shot modeling of NIF DT-layered ignition experiments. These simulations have attempted to include as much as practicable all of the effects known and believed to be important in determining the performance of NIF ignition experiments. These effects include both adjusting the incident x-ray flux applied to drive the capsule so as to reproduce the measured implosion dynamics, as well as including measured capsule surface finishes as seeds to instability growth and using adequate resolution to model the growth of the dominant unstable wavelengths. Across the ensemble of ignition experiments simulated from 2012, the simulations can be adjusted to match reasonably well the observed neutron down-scatter ratio, a measure of the compression achieved in the fuel, and in so doing also approximately match the hot spot size as extracted from x-ray self-emission measurements. For some shots simulated, the simulated ion temperature agrees reasonably well with that inferred from the Doppler-broadened primary neutron spectrum; however, for some shots it is considerably lower than simulated. Similarly, the yield is consistently lower than simulated, in some cases by a factor of three when α-particle deposition is switched off in simulations, while in others by more than an order of magnitude when α-particle deposition is included. Finally, a full sphere 3-D simulation of a selected shot (N120205) was run to assess if the influence of 3-D effects could resolve the persistent yield discrepancy. While a

number of the observables trend closer to the data in the 3-D simulation as compared to 2-D, the yield discrepancy remains substantial, indicating that other effects beyond three-dimensionality must be playing significant roles.

ACKNOWLEGEMENTS

This work was performed under the auspices of the U.S. Department of Energy by Lawrence Livermore National Laboratory under Contract DE-AC52-07NA27344.

REFERENCES

[1] A. J. Mackinnon, J. L. Kline, S. N. Dixit, S. H. Glenzer, M. J. Edwards, D. A. Callahan, N. B. Meezan, S. W. Haan, J. D. Kilkenny, T. Döppner, D. R. Farley, J. D. Moody, J. E. Ralph, B. J. MacGowan, O. L. Landen, H. F. Robey, T. R. Boehly, P. M. Celliers, J. H. Eggert, K. Krauter, G. Frieders, G. F. Ross, D. G. Hicks, R. E. Olson, S. V. Weber, B. K. Spears, J. D. Salmonsen, P. Michel, L. Divol, B. Hammel, C. A. Thomas, D. S. Clark, O. S. Jones, P. T. Springer, C. J. Cerjan, G. W. Collins, V. Y. Glebov, J. P. Knauer, C. Sangster, C. Stoeckl, P. McKenty, J. M. McNaney, R. J. Leeper, C. L. Ruiz, G. W. Cooper, 8 A. G. Nelson, 8 G. G. A. Chandler, K. D. Hahn, M. J. Moran, M. B. Schneider, N. E. Palmer, R. M. Bionta, E. P. Hartouni, S. LePape, P. K. Patel, N. Izumi, R. Tommasini, E. J. Bond, J. A. Caggiano, R. Hatarik, G. P. Grim, F. E. Merrill, D. N. Fittinghoff, N. Guler, O. Drury, D. C. Wilson, H. W. Herrmann, W. Stoeffl, D. T. Casey, M. G. Johnson, J. A. Frenje, R. D. Petrasso, A. Zylestra, H. Rinderknecht, D. H. Kalantar, J. M. Dzenitis, P. Di Nicola, D. C. Eder, W. H. Courdin, G. Gururangan, S. C. Burkhart, S. Friedrich, D. L. Blueuel, l. A. Bernstein, M. J. Eckart, D. H. Munro, S. P. Hatchett, A. G. Macphee, D. H. Edgell, D. K. Bradley, P. M. Bell, S. M. Glenn, N. Simanovskaia, M. A. Barrios, R. Benedetti, G. A. Kyrala, R. P. J. Town, E. L. Dewald, J. L. Milovich, K. Widmann, A. S. Moore, 7 G. LaCaille, S. P. Regan, L. J. Suter, B. Felker, R. C. Ashabranner, M. C. Jackson, R. Prasad, M. J. Richardson, T. R. Kohut, P. S. Datte, G. W. Krauter, J. J. Klingman, R. F. Burr, T. A. Land, M. R. Hermann, D. A. Latray, R. L. Saunders, S. Weaver, S. J. Cohen, L. Berzins, S. G. Brass, E. S. Palma, R. R. Lowe-Webb, G. N. McHalle, P. A. Arnold, L. J. Lagin, C. D. Marshall, G. K. Brunton, D. G. Mathisen, R. D. Wood, J. R. Cox, R. B. Ehrlich, K. M. Knittel, M. W. Bowers, R. A. Zacharias, B. K. Young, J. P. Holder, J. R. Kimbrough, T. Ma, K. N. La Fortune, C. C. Widmayer, M. J. Shaw, G. V.

Erbert, K. S. Jancaitis, J. M. DiNicola, C. Orth, G. Heestand, R. Kirkwood, C. Haynam, P. J. Wegner, P. K. Whitman, A. Hamza, E. G. Dzenitis, R. J. Wallace, S. D. Bhandarkar, T. G. Parham, R. Dylla-Spears, E. R. Mapoles, B. J. Kozioziemski, J. D. Sater, C. F. Walters, B. J. Haid, J. Fair, A. Nikroo, E. Giraldez, K. Moreno, B. Vanwonterghem, R. L. Kauffman, S. Batha, D. W. Larson, R. J. Fortner, D. H. Schneider, J. D. Lindl, R. W. Patterson, L. J. Atherton, and E. I. Moses, Phys. Rev. Lett. **108**, 215005 (2012).

[2] S. H. Glenzer, D. A. Callahan, A. J. MacKinnon, J. L. Kline, G. Grim, E. T. Alger, R. L. Berger, L. A. Bernstein, R. Betti, D. L. Bleuel, T. R. Boehly, D. K. Bradley, S. C. Burkhart, R. Burr, J. A. Caggiano, C. Castro, D. T. Casey, C. Choate, D. S. Clark, P. Celliers, C. J. Cerjan, G. W. Collins, E. L. Dewald, P. DiNicola, J. M. DiNicola, L. Divol, S. Dixit, T. Do¨ppner, R. Dylla-Spears, E. Dzenitis, M. Eckart, G. Erbert, D. Farley, J. Fair, D. Fittinghoff, M. Frank, L. J. A. Frenje, S. Friedrich, D. T. Casey, M. Gatu Johnson, C. Gibson, E. Giraldez, V. Glebov, S. Glenn, N. Guler, S. W. Haan, B. J. Haid, B. A. Hammel, A. V. Hamza, C. A. Haynam, G. M. Heestand, M. Hermann, H. W. Hermann, D. G. Hicks, D. E. Hinkel, J. P. Holder, D. M. Holunda, J. B. Horner, W. W. Hsing, H. Huang, N. Izumi, M. Jackson, O. S. Jones, D. H. Kalantar, R. Kauffman, J. D. Kilkenny, R. K. Kirkwood, J. Klingmann, T. Kohut, J. P. Knauer, J. A. Koch, B. Kozioziemki, G. A. Kyrala, A. L. Kritcher, J. Kroll, K. La Fortune, L. Lagin, O. L. Landen, D. W. Larson, D. LaTray, R. J. Leeper, S. Le Pape, J. D. Lindl, R. Lowe-Webb, T. Ma, J. McNaney, A. G. MacPhee, T. N. Malsbury, E. Mapoles, C. D. Marshall, N. B. Meezan, F. Merrill, P. Michel, J. D. Moody, A. S. Moore, M. Moran, K. A. Moreno, D. H. Munro, B. R. Nathan, A. Nikroo, R. E. Olson, C. D. Orth, A. E. Pak, P. K. Patel, T. Parham, R. Petrasso, J. E. Ralph, H. Rinderknecht, S. P. Regan, H. F. Robey, J. S. Ross, M. D. Rosen, R. Sacks, J. D. Salmonson, R. Saunders, J. Sater, C. Sangster, M. B. Schneider, F. H. Se´guin, M. J. Shaw, B.

K. Spears, P. T. Springer, W. Stoeffl, L. J. Suter, C. A. Thomas, R. Tommasini, R. P. J. Town, C. Walters, S. Weaver, S. V. Weber, P. J. Wegner, P. K. Whitman, K. Widmann, C. C. Widmayer, C. H. Wilde, D. C. Wilson, B. Van Wonterghem, B. J. MacGowan, L. J. Atherton, M. J. Edwards, and E. I. Moses, Phys. Plasmas **19**, 056318 (2012).

[3] G. H. Miller, E. I. Moses, and C. R. Wuest, Nuc. Fusion **44**, S228 (2004).

[4] S. W. Haan, J. D. Lindl, D. A. Callahan, D. S. Clark, J. D. Salmonson, B. A. Hammel, L. J. Atherton, R. C. Cook, M. J. Edwards, S. Glenzer, A. V. Hamza, S. P. Hatchett, M. C. Herrmann, D. E. Hinkel, D. D. Ho, H. Huang, O. S. Jones, J. Kline, G. Kyrala, O. L. Landen, B. J. MacGowan, M. M. Marinak, D. D. Meyerhofer, J. L. Milovich, K. A. Moreno, E. I. Moses, D. H. Munro, A. Nikroo, R. E. Olson, K. Peterson, S. M. Pollaine, J. E. Ralph, H. F. Robey, B. K. Spears, P. T. Springer, L. J. Suter, C. A. Thomas, R. P. Town, R. Vesey, S. V. Weber, H. L. Wilkens, and D. C. Wilson, Phys. Plasmas **18**, 051001 (2011).

[5] J. D. Lindl, P. A. Amendt, R. L. Berger, S. G. Glendinning, S. H. Glenzer, S. W. Haan, R. L. Kauffman, O. L. Landen, and L. J. Suter, Phys. Plasmas **11**, 339 (2004).

[6] S. Atzeni and J. Meyer-ter-Vehn *The Physics of Inertial Fusion* (Clarendon, Oxford, 2004).

[7] R. P. J. Town, M. D. Rosen, P. A. Michel, L. Divol, J. D. Moody, G. A. Kyrala, M. B. Schneider, J. L. Kline, C. A. Thomas, J. L. Milovich, D. A. Callahan, N. B. Meezan, D. E. Hinkel, E. A. Williams, R. L. Berger, M. J. Edwards, L. J. Suter, S. W. Haan, J. D. Lindl, E. L. Dewald, S. Dixit, S. H. Glenzer, O. L. Landen, E. I. Moses, H. A. Scott, J. A. Harte, and G. B. Zimmerman, Phys. Plasmas **18**, 056302 (2010).

[8] Lord Rayleigh, *Scientific Papers* (Cambridge University Press, Cambridge, England, 1900).

[9] G. I. Taylor, Proc. R. Soc. London, Ser. A **201**, 192 (1950).

[10] R. D. Richtmyer, Commun. Pure Appl. Math. **13**, 297 (1960).

[11] E. E. Meshkov, Fluid Dyn. **4**, 101 (1969).

[12] J. Edwards, M. Marinak, T. Dittrich, S. Haan, J. Sanches, J. Klingmann, and J. Moody, Phys. Plasmas **12**, 056318 (2005).

[13] B. A. Hammel, S. W. Haan, D. S. Clark, M. J. Edwards, S. H. Langer, M. M. Marinak, M. V. Patel, J. D. Salmonson, and H. A. Scott, High Energy Density Physics **6**, 171 (2010).

[14] D. S. Clark, S. W. Haan, J. D. Salmonson, Phys. Plasmas **15**, 056305 (2008).

[15] D. S. Clark, S. W. Haan, A. W. Cook, M. J. Edwards, B. A. Hammel, J. M. Koning, and M. M. Marinak, Phys. Plasmas **18**, 082701 (2011).

[16] O. S. Jones, C. J. Cerjan, M. M. Marinak, J. L. Milovich, H. F. Robey, P. T. Springer, L. R. Benedetti, D. L. Bleuel, E. J. Bond, D. K. Bradley, D. A. Callahan, J. A. Caggiano, P. M. Celliers, D. S. Clark, S. M. Dixit, T. Döppner, R. J. Dylla-Spears, E. G. Dzentitis, D. R. Farley, S. M. Glenn, S. H. Glenzer, S. W. Haan, B. J. Haid, C. A. Haynam, D. G. Hicks, B. J. Kozioziemski, K. N. LaFortune, O. L. Landen, E. R. Mapoles, A. J. MacKinnon, J. M. McNaney, N. B. Meezan, P. A. Michel, J. D. Moody, M. J. Moran, D. H. Munro, M. V. Patel, T. G. Parham, J. D. Sater, S. M. Sepke, B. K. Spears, R. P. J. Town, S. V. Weber, K. Widmann, C. C. Widmayer, E. A. Williams, L. J. Atherton, M. J. Edwards, J. D. Lindl, B. J. MacGowan, L. J. Suter, R. E. Olson, H. W. Herrmann, J. L. Kline, G. A. Kyrala, D. C. Wilson, J. Frenje, T. R. Boehly, V. Glebov, J. P. Knauer, A. Nikroo, H. Wilkens, and J. D. Kilkenny, Phys. Plasmas **19**, 056315 (2012).

[17] T. R. Boehly, D. Munro, P. M. Celliers, R. E. Olson, D. G. Hicks, V. N. Goncharov, G. W. Collins, H. F. Robey, S. X. Hu, J. A. Morozas, T. C. Sangster, O. L. Landen, and D. D. Meyerhofer, Phys. Plasmas **16**, 056302 (2009).

[18] H. F. Robey, T. R. Boehly, P. M. Celliers, J. H. Eggert, D. Hicks, R. F. Smith, R. Collins, M. W. Bowers, K. G. Krauter, P. S. Datte, D. H. Munro, J. L. Milovich, O. S. Jones, P. A. Michel, C. A. Thomas, R. E. Olson, S. Pollaine, R. P. J. Town, S. Haan, D. Callahan, D. Clark, J. Edwards, J. L. Kline, S. Dixit, M. B. Schneider, E. L. Dewald, K. Widmann, J. D. Moody, T. Döppner, H. B. Radousky, A. Throop, D. Kalantar, P. DiNicola, A. Nikroo, J. J. Kroll, A. V. Hamza, J. B. Horner, S. D. Bhandarkar, E. Dzenitis, E. Alger, E. Giraldez, C. Castro, K. Moreno, C. Haynam, K. N. LaFortune, C. Widmayer, M. Shaw, K. Jancaitis, T. Parham, D. M. Holunga, C. F. Walters, B. Haid, E. R. Mapoles, J. Sater, C. R. Gibson, T. Malsbury, J. Fair, D. Trummer, K. R. Coffee, B. Burr, L. V. Berzins, C. Choate, S. J. Brereton, S. Azevedo, H. Chandrasekaran, D. C. Eder, N. D. Masters, A. C. Fisher, P. A. Sterne, B. K. Young, O. L. Landen, B. M. Van Wonterghem, B. J. MacGowan, J. Atherton, J. D. Lindl, D. D. Meyerhofer, and E. Moses, Phys. Plasmas **19**, 042706 (2012).

[19] D. G. Hicks, B. K. Spears, D. G. Braun, R. E. Olson, C. M. Sorce, P. M. Celliers, G. W. Collins, and O. L. Landen, Phys. Plasmas **17**, 102703 (2010).

[20] D. G. Hicks, N. B. Meezan, E. L. Dewald, A. J. Mackinnon, D. A. Callahan, T. Döppner, L. R. Benedetti, D. K. Bradley, P. M. Celliers, D. S. Clark, S. N. Dixit, E. G. Dzenitis, J. E. Eggert, D. R. Farley, S. M. Glenn, S. H. Glenzer, A. V. Hamza, R. F. Heeter, J. P. Holder, N. Izumi, D. H. Kalantar, S. F. Khan, J. J. Kroll, T. Ma, A. G. MacPhee, J. M. McNaney, J. D. Moody, M. J. Moran, B. R. Nathan, K. P. Opachich, R. R. Prasad, J. E. Ralph, H. F. Robey, J. R. Rygg, J. D. Salmonson, M. B. Schneider, N. Simanovskaia, B. K. Spears, R. Tommasini, K. Widmann, G. W. Collins, O. L. Landen, J. D. Kilkenny, W. W. Hsing, B. J. MacGowan, L. J. Atherton, M. J. Edwards, R. E. Olson, J. A Frenje, R. D. Petrasso, H. G. Rinderknecht, A. B. Zylstra, J. L Kline, G. A. Kyrala, and A. Nikroo, submitted to *Phys. Plasmas*.

[21] M. M. Marinak, G. D. Kerbel, N. A. Gentile, O. Jones, D. Munro, S. Pollaine, T. R. Dittrich, and S. W. Haan, Phys. Plasmas **8**, 2275 (2001).

[22] J. A. Frenje, D. T. Casey, C. K. Li, F. H. Séguin, R. D. Petrasso, V. Yu Glebov, P. B. Radha, T. C. Sangster, D. D. Meyerhofer, S. P. Hatchett, S. W. Haan, C. J. Cerjan, O. L. Landen, K. A. Fletcher, and R. J. Leeper, Phys. Plasmas **17**, 056311 (2010).

[23] B. J. Kozioziemski, E. R. Mapoles, J. D. Sater, A. A. Chernov, J. D. Moody, J. B. Lugten, and M. A. Johnson, Fusion Sci. Technology **59**, 14 (2011).

[24] H. Huang, R. B. Stephens, J. B. Gibson, and I. Valmainski, Fusion Sci. Technology **49**, 642 (2006).

[25] A. Q. L. Nguyen, S. A. eddinger, H. Huang, M. A. Johnson, Y. T. Lee, R. C. Montesanti, K. A. Moreno, and M. E. Schoff, Fusion Sci. Technology **55**, 399 (2009).

[26] B. A. Hammel, H. A. Scott, S. P. Regan, C. Cerjan, D. S. Clark, M. J. Edwards, R. Epstein, S. H. Glenzer, S. W. Haan, N. Izumi, J. A. Koch, G. A. Kyrala, O. L. Landen, S. H. Langer, K. Peterson, V. A. Smalyuk, L. J. Suter, and D. C. Wilson, Phys. Plasmas **18**, 056310 (2011).

[27] G. Grim, *et al*., Phys. Plasmas, this issue.

[28] J. P. Knauer, *et al*., Phys. Plasmas, this issue.

[29] C. Cerjan, *et al*., Phys. Plasmas, this issue

[30] B. K. Spears, D. S. Clark, M. J. Edwards, S. W. Haan, J. D. Lindl, D. H. Munro, L. J. Suter, and C. A. Thomas, Bull. Am. Phys. Soc. **57**, 112 (2012).

[31] R. H. H. Scott, D. S. Clark, D. K. Bradley, D. A. Callahan, M. J. Edwards, S. W. Haan, M. M. Marinak, R. P. J. Town, P. A. Norreys, and L. J. Suter, Bull. Am. Phys. Soc. **57**, 247 (2012).

Table 1. 2012 NIF ignition experiments simulated in this study.

shot number	description	laser power	dopant	DSR (%)	T_{ion} (keV)	neutron yield
N120126	slow-rise (3 ns), coasting, Au hohl.	419 TW	2% Si	3.92±0.16	2.9±0.09	3.2×10^{14}
N120131	fast-rise (1 ns), coasting, Au hohl.	418 TW	2% Si	3.67±0.17	4.0±0.15	5.8×10^{14}
N120205	slow-rise (3 ns), coasting, Au hohl.	419 TW	2% Si	4.30±0.19	3.3±0.15	5.6×10^{14}
N120213	slow-rise (3 ns), coasting, DU hohl.	425 TW	2% Si	4.25±0.24	1.9±1.6	9.6×10^{13}
N120311	slow-rise (3 ns), no-coast, DU hohl.	334 TW	2% Si	4.93±0.26	2.0±0.09	3.5×10^{14}
N120321	slow-rise (3 ns), no-coast, DU hohl.	331 TW	4% Si	6.26±0.46	3.1±0.14	4.2×10^{14}
N120405	slow-rise (3ns), no-coast, DU hohl.	387 TW	4% Si	5.14±0.29	1.7±0.13	1.3×10^{14}

Table 2. Simulated outputs for three different 2-D realizations of N120205.

	realization #1	realization #2	realization #3	expt.
P_0 (μm)	25.36	28.28	26.25	22.89
P_2/P_0	- 0.03	- 0.11	- 0.09	- 0.15
P_3/P_0	0.03	0.02	- 0.01	0.00
P_4/P_0	0.04	0.03	0.03	0.02
DSR (%)	4.60	4.36	4.35	4.54
T_{ion} (keV)	2.91	2.98	2.99	3.39
neutrons (10^{14})	17.8	17.4	18.3	5.64

Table 3. Summary of simulated outputs for N120205: 1-D, 2-D, and 3-D.

	α-particle deposition on			α-particle deposition off			
	1-D	2-D	3-D	1-D	2-D	3-D	expt.
fuel vel. (km/s)	297.8	299.1	—	297.8	299.1	—	—
fuel adiabat	1.65	1.65	—	1.65	1.65	—	—
abl. frac. remaining (%)	14.6	14.2	—	14.6	14.2	—	—
P_0 (μm)	24.8	26.22	25.1	24.8	24.2	26.8	22.89
P_2/P_0	—	- 0.04	- 0.27	—	- 0.05	- 0.24	- 0.15
DSR (%)	4.47	4.67	4.92	4.41	4.60	4.24	4.30
T_{ion} (keV)	3.16	3.19	3.48	2.90	2.91	3.29	3.39
HS mass (μg)	15.7	15.6	14.2	15.2	13.0	11.0	4.80
HS density (g/cm^3)	74.5	81.8	71.1	80.9	71.6	52.8	44.2
HS pres. (Gbar)	194.1	202.4	178.6	176.6	161.2	131.4	102.1
res. kin. energy (kJ)	0.05	0.18	0.71	0.13	0.52	1.35	1.6 – 4.2
neutrons (10^{14})	39.2	29.8	23.6	22.9	17.8	16.2	5.6

FIGURE CAPTIONS

Fig. 1. (Color online) Adjusted 1-D x-ray drive used in capsule-only simulations for shot N120205 (a) that was matched to the VISAR shock timing from shot N120108 (b) and ConA measured implosion trajectory from shot N120122 (c). In (b) and (c), the red curves show the simulated data from the 1-D adjusted implosions, and the black trace and black points, respectively, represent the experimental data. The insets show example raw data.

Fig. 2. (Color online) Match to ConA observables from N120122 other than the implosion trajectory shown in Fig. 1(c). Shown in panels (a) – (d) are shell mass averaged implosion velocity, shell remaining mass, peak shell density, and shell thickness. In each panel, the red curve shows the result of the 1-D adjusted simulation, and the black points with error bars show the data. Aside from the late time shell remaining mass (b), and early time shell thickness (d), the agreement is fairly close between experiment and the adjusted simulation.

Fig. 3. (Color online) Example roughness power spectra used as hydrodynamic instability seeds in 2-D simulations for shot N120205. Panel (a) shows the ice roughness spectrum as a function of Legendre mode number measured from three views of the ice layer prior to shot (green, red, and blue curves). Also shown in black is the maximum allowed roughness according to ignition specifications. Panel (b) shows the outer ablator surface roughness as measured from eighteen meridian AFM traces and one equatorial trace. For comparison, the allowed roughness from the ignition specifications is also shown.

Fig. 4. (Color online) Imploded configurations at bang time from three realizations of the post-shot simulation for N120205. The upper half of each panel shows the material density and the lower half

shows the material regions. Dark blue corresponds to the DT fuel, and the other colors to the various doped ablator layers. The red contour demarcates the hot spot boundary.

Fig. 5. (Color online) Comparison of simulated and measured values for four principal experimental observables across the ensemble of post-shot simulations from 2012. Panels (a) – (d) show neutron down-scatter ratio (DSR), ion temperature inferred from the Doppler broadened primary neutron spectrum, hot spot size, and primary neutron yield as a function of shot number. In each panel the data are represented by the black symbols with error bars, and the simulated results are the red symbols. The error bars on the simulation results are the RMS variation between different roughness realizations used in simulations. In most cases, these error bars are smaller than the symbol size. These simulation results do not include α-particle deposition.

Fig. 6. (Color online) Comparison of simulated versus measured yield for the ensemble of shots simulated both with and without α-particle deposition included in the simulations. Panel (a) shows yield values versus shot number, and panel (b) shows the ratio of experimentally measured yield to 2-D simulation. The horizontal dashed lines in (b) give the average yield over simulated for the entire ensemble of shots.

Fig. 7. (Color online) Dependence of simulated observables for shot N120321 on increased ablator surface roughness relative to measured. Increasing the surface roughness by a factor of five brings the simulations into approximate agreement with the observed neutron yield, ion temperature, and hot spot size. Shell break up at this high roughness, however, degrades the simulated DSR well below observation. These simulations include α-particle deposition.

Fig. 8. (Color online) Dependence of simulated observables for shot N120321 on mass of pre-loaded ablator material mixed into the central DT gas. An injected mass of ~ 1,000 ng brings the simulated yield into agreement with observation but degrades the simulated ion temperature and hot spot size below the measured values. Radiative collapse in the hot spot for large mix masses increases the DSR well above the measurement. These simulations include α-particle deposition.

Fig. 9. (Color online) 3-D surface realizaitons in HYDRA for shot N120205. (a) shows the DT ice-gas interface including ice grooves, and (b) shows the ablator outer surface combining AFM and PSDI surface characterization. The color scales show the radial deviation in height along the surface.

Fig. 10. (Color online) 3-D simulation of N120205 at bang time. The cutaway green surface shows the fuel-ablator interface, and the enclosed red surface shows the 1 keV ion temperature isosurface, an effective indicator of the boundary between the low density hot spot and high density cold, compressed fuel. The large, spike-like deviations in the fuel-ablator interface correspond to large, localized defects in the initial ablator surface.

Fig. 11. (Color online) 2-D slice through the 3-D simulation in Fig. 10 aligned with the hohlraum axis (a). The color scale gives the density. The corresponding 2-D simulation result is shown in (b) on the same color scale. Larger Rayleigh-Taylor spikes penetrating the hot spot are apparent in the 3-D simulation than in 2-D as well as larger bubbles rising into the dense shell.

Fig. 12. (Color online) 2-D slice analogous to Fig. 11 showing flow speed in the hot spot. Nearly twice the peak flow velocity is reached in the 3-D simulation compared to 2-D representing implosion kinetic energy that is not effectively converted into fuel compression or hot spot heating. More fine-scale, turbulent-like features are also apparent in the 3-D result that are absent in the 2-D equivalent.

Fig. 1

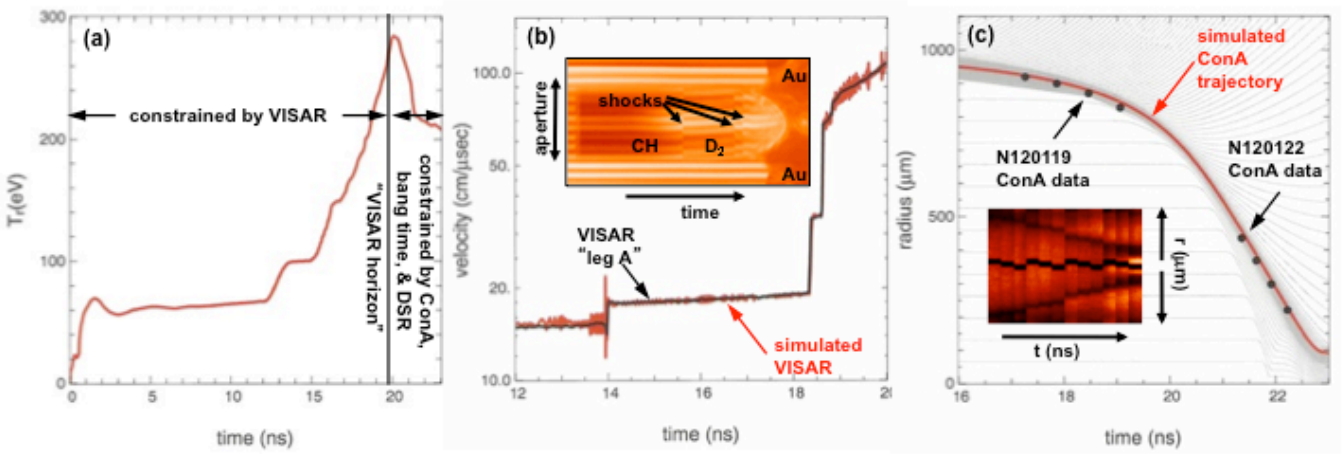
(a)
constrained by VISAR
"VISAR horizon"
constrained by ConA, bang time, & DSR
T_r(eV)
time (ns)
(b)
shocks
Au
CH
D_2
Au
aperture
time
VISAR "leg A"
simulated VISAR
velocity (cm/μsec)
time (ns)
(c)
simulated ConA trajectory
N120119 ConA data
N120122 ConA data
r (μm)
t (ns)
radius (μm)
time (ns)

Fig. 2

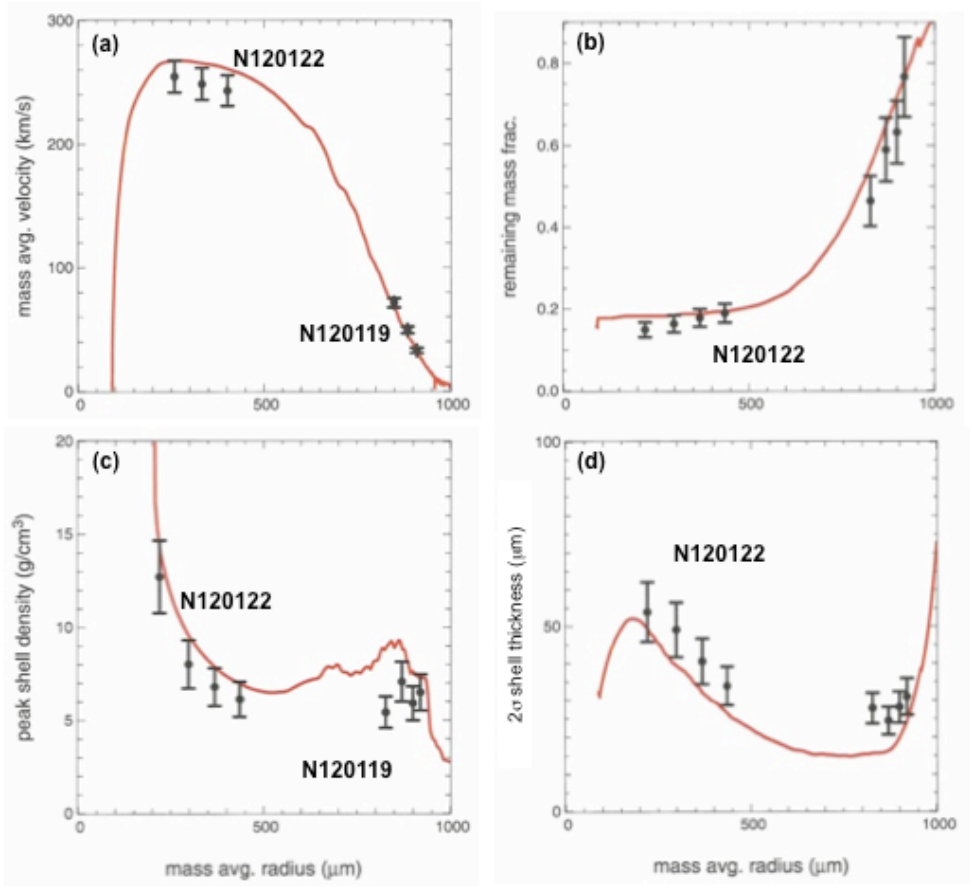
(a)
N120122
N120119
mass avg. velocity (km/s)
(b)
N120122
remaining mass frac.
(c)
N120122
N120119
peak shell density (g/cm³)
mass avg. radius (μm)
(d)
N120122
2σ shell thickness (μm)
mass avg. radius (μm)

Fig. 3

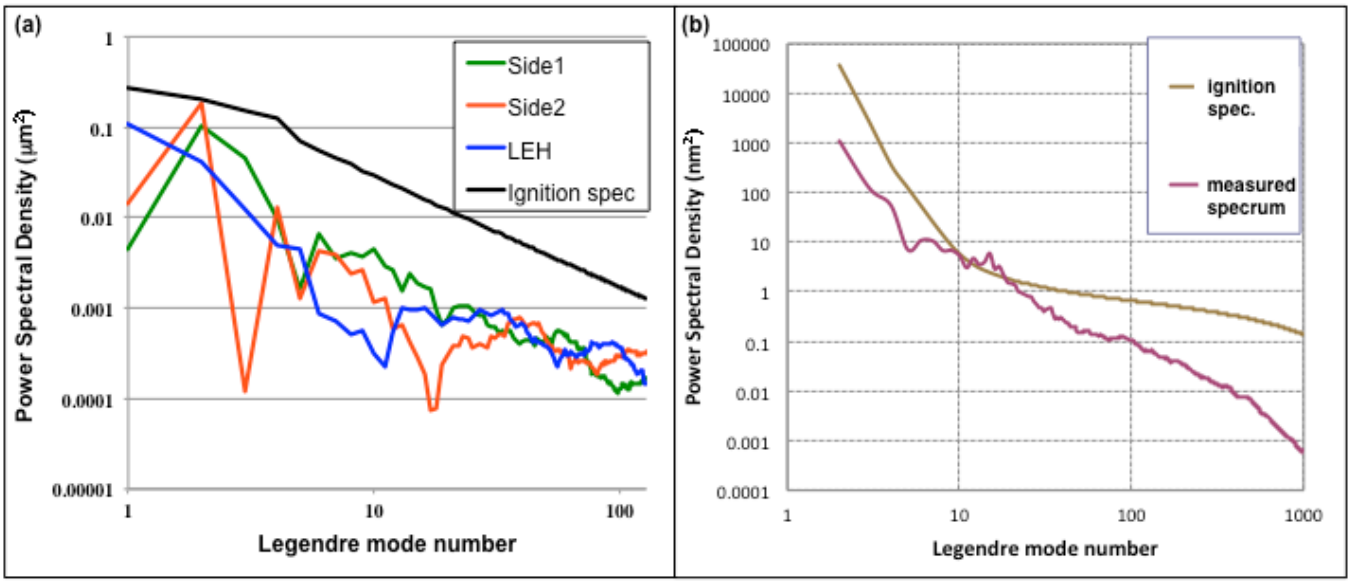
(a)
Power Spectral Density (μm²)
1
0.1
0.01
0.001
0.0001
0.00001
1
10
100
Legendre mode number
Side1
Side2
LEH
Ignition spec
(b)
Power Spectral Density (nm²)
100000
10000
1000
100
10
1
0.1
0.01
0.001
0.0001
1
10
100
1000
Legendre mode number
ignition spec.
measured specrum

Fig. 4

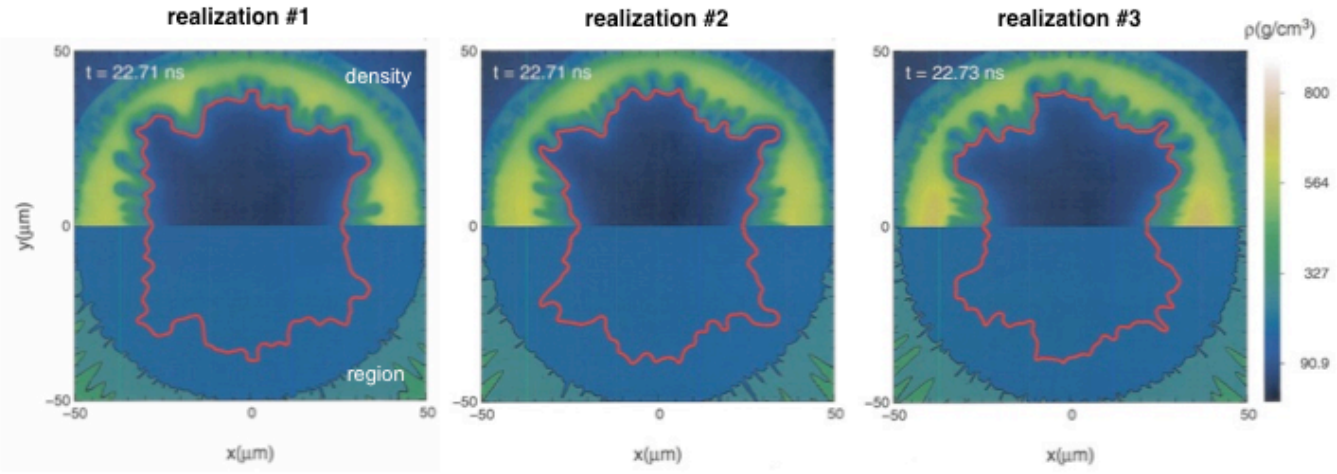
realization #1
realization #2
realization #3
ρ(g/cm³)
t = 22.71 ns
density
region
t = 22.71 ns
t = 22.73 ns
800
564
327
90.9
y(μm)
x(μm)
x(μm)
x(μm)
50
0
−50

Fig. 5

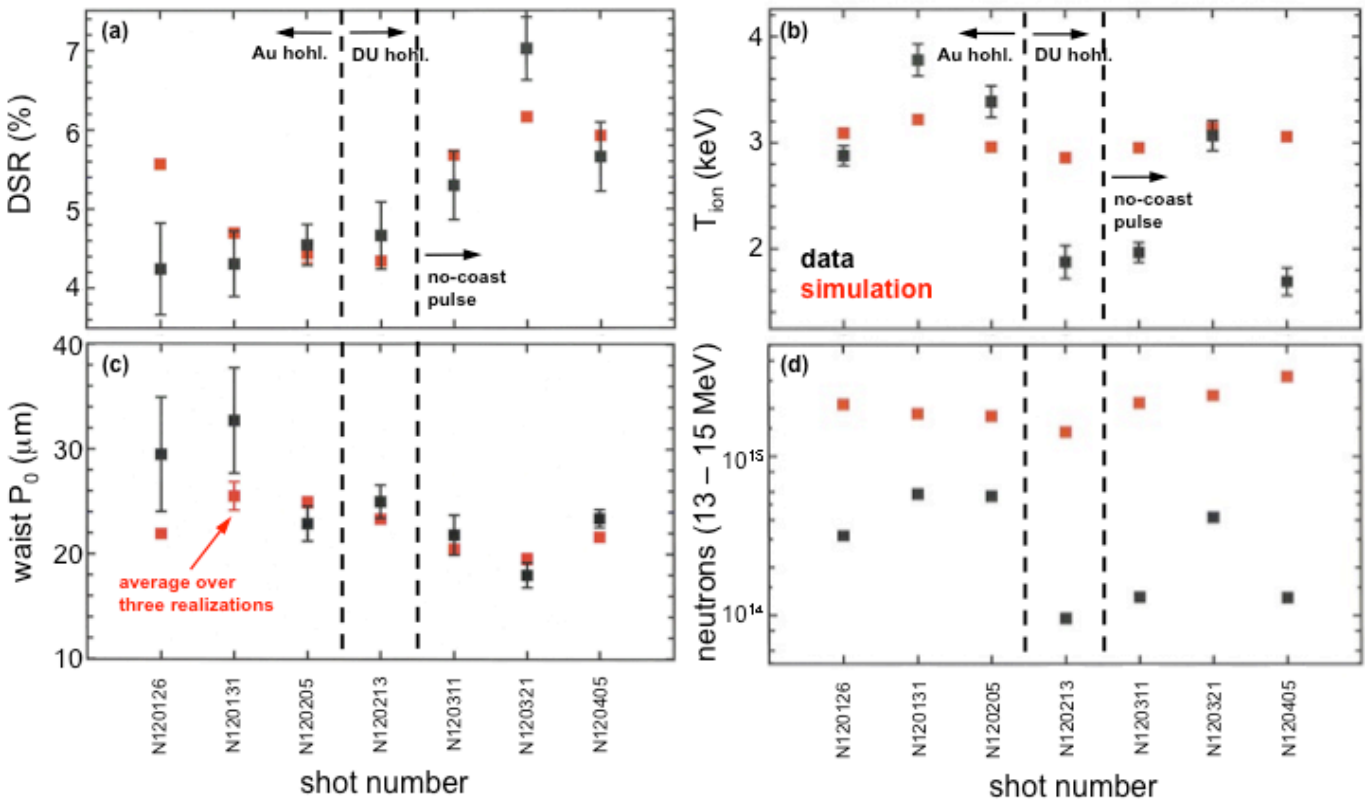
(a)
Au hohl.
DU hohl.
no-coast pulse
DSR (%)
(b)
data
simulation
T_{ion} (keV)
(c)
waist P_0 (μm)
average over three realizations
(d)
neutrons (13 – 15 MeV)
N120126
N120131
N120205
N120213
N120311
N120321
N120405
shot number

Fig. 6

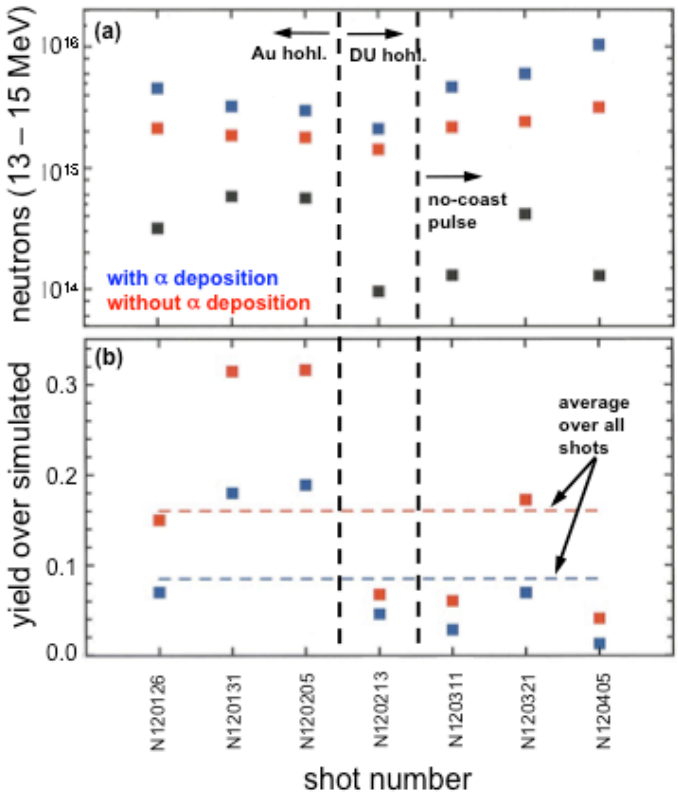
(a)
Au hohl.
DU hohl.
no-coast pulse
with α deposition
without α deposition
neutrons (13 – 15 MeV)
10^16
10^15
10^14
(b)
yield over simulated
0.3
0.2
0.1
0.0
average over all shots
N120126
N120131
N120205
N120213
N120311
N120321
N120405
shot number

Fig. 7

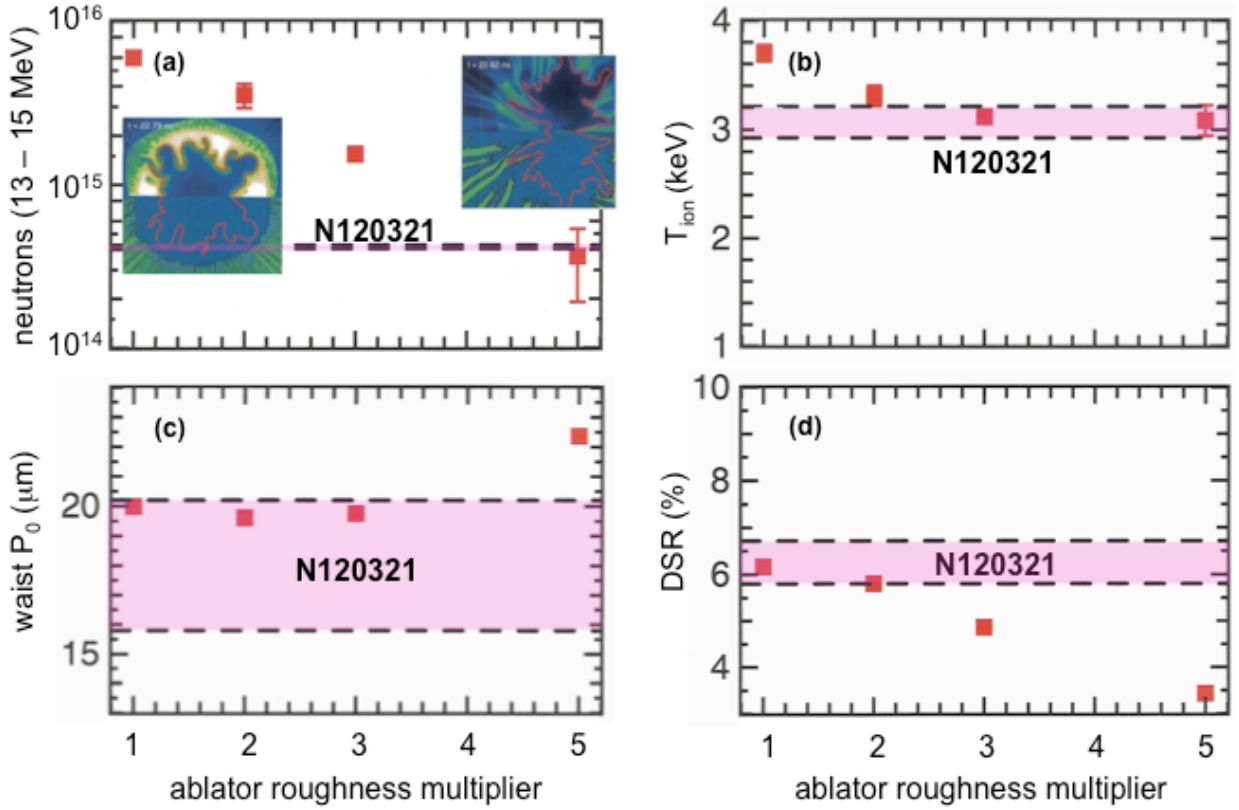
(a)
(b)
(c)
(d)
neutrons (13 – 15 MeV)
T_{ion} (keV)
waist P_0 (μm)
DSR (%)
N120321
ablator roughness multiplier

Fig. 8

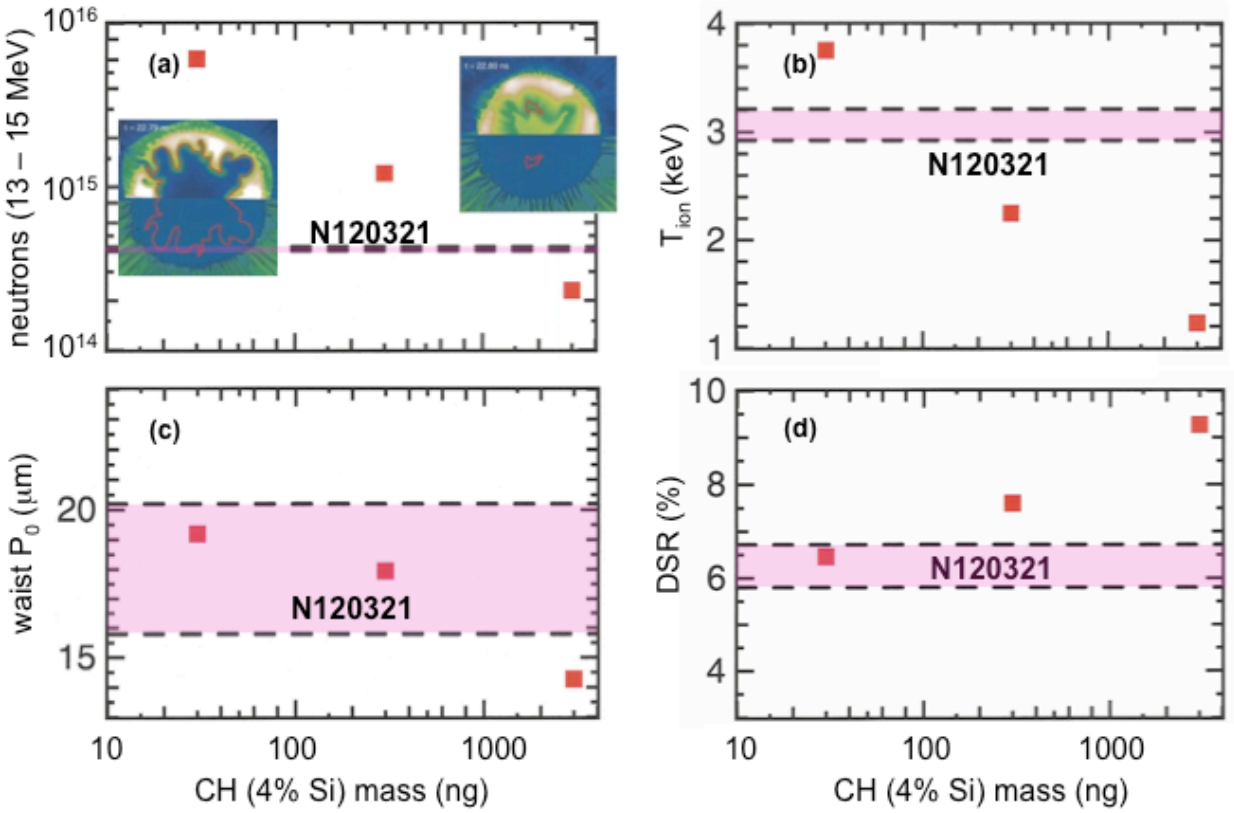
(a)
(b)
(c)
(d)
neutrons (13 – 15 MeV)
10^{16}
10^{15}
10^{14}
T_{ion} (keV)
waist P_0 (μm)
DSR (%)
N120321
CH (4% Si) mass (ng)
10
100
1000

Fig. 9

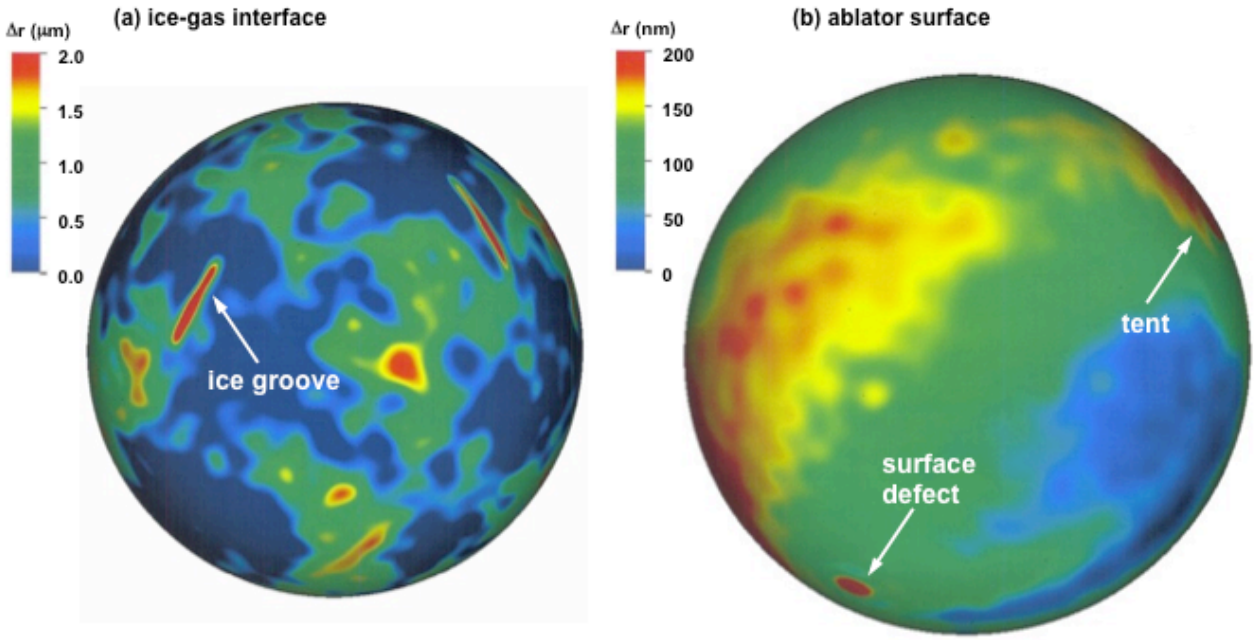
(a) ice-gas interface
Δr (μm)
2.0
1.5
1.0
0.5
0.0
ice groove
(b) ablator surface
Δr (nm)
200
150
100
50
0
tent
surface
defect

Fig. 10

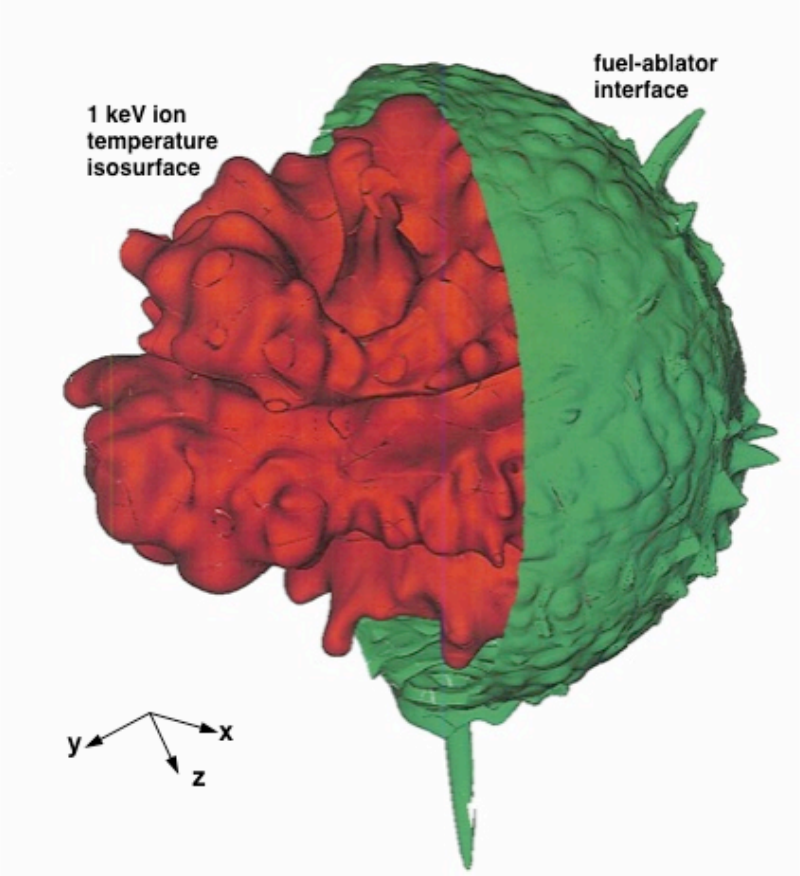
fuel-ablator
interface
1 keV ion
temperature
isosurface
y
x
z

Fig. 11

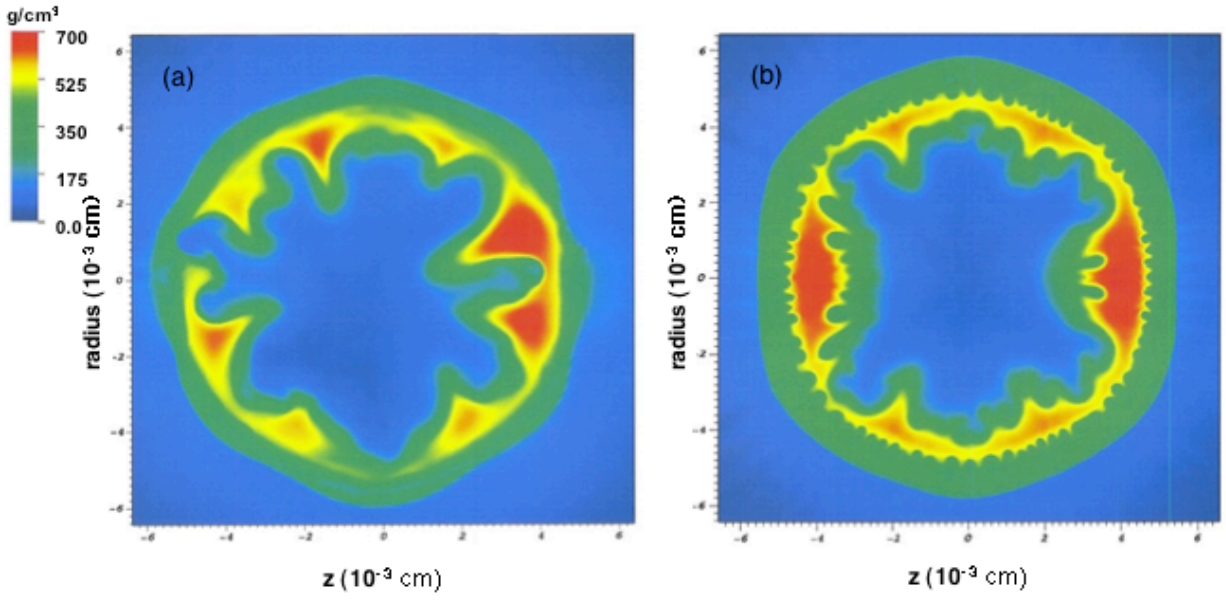

Fig. 12